Materials Advances

ROYAL SOCIETY OF CHEMISTRY

PAPER

View Article Online
View Journal | View Issue

Cite this: *Mater. Adv.*, 2025, **6**, 3546

Microstructural, mechanical, corrosion, and biological behavior of spark plasma sintered commercially pure zinc for biomedical applications

Mayank Kumar Yadav,[a] Riddhi Hirenkumar Shukla,[a] K. Praveenkumar,[b] Sagar Nilawar,[c] Chandra Sekhar Perugu,[d] Prabhukumar Sellamuthu,[e] Kaushik Chatterjee,[c] Satyam Suwas,[c] J. Jayaraj[fg] and K. G. Prashanth*[ah]

This study investigates the microstructural, mechanical, corrosion, and biological behaviors of spark plasma sintered (SPS) zinc (Zn) samples for biomedical applications. The findings reveal that SPS significantly refines the grain structure of pure Zn compared to the conventional casting method. The SPS process, conducted at a lower sintering temperature of 300 °C and a high uniaxial pressure of 50 MPa, produces fine and uniform equiaxed grains with an average size of 19 μm. The resulting Zn samples exhibit a calculated density of 7.1 g cc^{-1} due to complete densification. The sintering process disrupts the initial texture strength, and the uniform grain orientation achieved during SPS contributes to an isotropic microstructure, enhancing the mechanical properties. The compressive yield strength and ultimate strength of the SPS samples are 115 ± 4 MPa and 191 ± 6 MPa, respectively. The long-term biodegradation behavior of SPS Zn in simulated body fluid indicates controlled and gradual corrosion, supporting its potential for biodegradable implant applications, while potentiodynamic polarization analysis further confirms similar corrosion rates compared to cast Zn due to the formation of a stable corrosion product film. *In vitro* studies with MC3T3-E1 preosteoblast cells show healthy proliferation in culture media containing the degradation products of SPS Zn. Due to its unique microstructural, mechanical, and corrosion properties, along with its biocompatibility, SPS-processed Zn is a promising candidate for tissue engineering applications.

Received 2nd February 2025,
Accepted 11th April 2025

DOI: 10.1039/d5ma00092k

rsc.li/materials-advances

A. Introduction

Recent studies have highlighted the growing demand for biodegradable implants in tissue engineering applications.[1–4] Among various biodegradable materials such as magnesium (Mg), zinc (Zn), and iron (Fe), Zn and their alloys stand out due to their promising features like biodegradability, biocompatibility, lower energy consumption during sintering, and favorable mechanical properties.[5–7] However, as-cast Zn often exhibits a coarse microstructure, resulting in low mechanical strength and pronounced anisotropy.[8] Clinical challenges like stress shielding and the need for secondary surgery make biodegradable materials a viable alternative to permanent materials such as titanium (Ti), stainless steel (SS), and cobalt–chromium (CoCr) alloys in tissue engineering applications.[9–14] Biodegradable or bioresorbable metals are a special class of materials that gradually degrade or resorb, allowing new cells to form functional tissues when placed at a diseased site.[1] These materials provide initial mechanical support to diseased organs or tissues and are gradually resorbed by biological fluids, facilitating bone tissue regeneration at critical-sized bone defect sites.[15] This approach mitigates issues like long-term damage or the need for secondary surgery associated with permanent metallic implants. Mg, Zn, and Fe are commonly used degradable metals.[15–18] Among these, Mg has a Young's modulus like natural bone but

[a] *Department of Mechanical and Industrial Engineering, Tallinn University of Technology, Ehitajate tee 5, 19086 Tallinn, Estonia. E-mail: kgprashanth@gmail.com, prashanth.konda@taltech.ee*
[b] *Faculty of Materials Science and Technology, VSB—Technical University of Ostrava, 17. listopadu 2172/15, 70 800 Ostrava, Czech Republic*
[c] *Department of Materials Engineering, Indian Institute of Science (IISc), Bangalore 560012, India*
[d] *Emerging Nanoscience Research Institute (EnRI), Nanyang Technological University, 50 Nanyang Avenue, 639798, Singapore*
[e] *Department of Mechanical Engineering, Presidency University, Bangalore, India*
[f] *Materials Technology, Dalarna University, SE-79188, Falun, Sweden*
[g] *Department of Mechanical and Materials Engineering, Karlstad University, SE-65188, Karlstad, Sweden*
[h] *Centre for Biomaterials, Cellular and Molecular Theranostics (CBCMT), Vellore Institute of Technology, School of Mechanical Engineering, Tamil Nadu, 632014, India*

degrades rapidly in physiological environments, increasing local alkalinity and forming hydrogen pockets affecting the healing process.[19–24] Fe, on the other hand, degrades too slowly and remains in the body for extended periods.[25] Zn's corrosion potential (−0.8 V) lies between that of Mg (∼−2.4 V) and Fe (−0.4 V), resulting in a degradation rate that aligns well with tissue generation.[26,27]

As an essential metallic element, Zn plays a crucial role in bone metabolism, to stimulate the formation of osteoblasts and inhibit osteoclast differentiation, thus enhancing bone strength.[28,29] Consequently, biodegradable Zn alloys offer significant advantages over biodegradable materials (polymers, Mg, and Fe-based alloys) in orthopedic applications.[30,31] For instance, Bowen *et al.*[32,33] investigated the *in vivo* biodegradation behavior by inserting pure Zn wire into the arteries of rats, which degraded at an optimal rate (20 μm per year) for biodegradable stents during the initial three months. Despite Zn's numerous suitable properties for biomedical applications, its use is limited due to the coarse microstructure of as-cast pure Zn offering poor mechanical strength and strong anisotropy.[34,35] Researchers have attempted to enhance Zn's properties through mechanical alloying or other similar processing techniques to reduce grain size and improve strength and ductility. Forming techniques such as rolling, forging, equal channel angular pressing (ECAP), high-pressure torsion (HPT), and additive manufacturing (AM) have been employed to refine Zn's microstructure.[36–39] For example, Wen *et al.*[18] optimized the selective laser melting (SLM) processing parameters to produce high-density pure Zn with enhanced mechanical properties (hardness of 46 ± 2 HV, Young's modulus of 20 ± 6 GPa, yield strength of 122 ± 3 MPa, ultimate strength of 138 ± 3 MPa, and elongation of 8 ± 1%). Similarly, Salehi *et al.*[40] used a two-step 3D printing technique to create Mg–5.9Zn–0.13Zr components, achieving functional parts with increased relative density (69 ± 0.5%) and compressive yield strength (31 ± 3 MPa) through liquid phase sintering. Lu and Li *et al.*[41,42] employed a high-pressure phase transition method to enhance the mechanical and corrosion behavior of Zn–1.5Mn and Zn–Li alloys through solid solution strengthening. Lin *et al.*[43] fabricated Mg_xZn_y/Zn composites *via* accumulative roll bonding (ARB), achieving enhanced mechanical properties, along with an enhanced elongation of 12%, and improved corrosion resistance after 15 cycles. Demirtas *et al.*[44] demonstrated that multiple equal channel extrusions reduced the grain size (2.0 mm) of Zn-0.3 wt% Al and the presence of Al-enriched precipitates, ranging from 50 to 200 nm, significantly enhancing the alloy's superplasticity at room temperature. Yang *et al.*[31] developed binary zinc-based materials with elements like Ca, Mg, Li, Sr, Fe, Mn, Ag, and Fe improving cytocompatibility, osteogenesis, and osseointegration. However, the selection and proportion of alloying elements must be carefully considered to achieve good biocompatibility.

Given the challenges of developing defect-free, fine microstructured pure Zn for tissue engineering applications, this research employs the spark plasma sintering (SPS) technique to produce dense and fine micro-structured Zn without alloying or mechanical processing. SPS is an advanced sintering methodology that applies uniaxial pressure and pulsed current to heat the powder, facilitating rapid densification at lower sintering temperatures.[45–49] The relatively fast cooling rate of SPS (compared to conventional cast) results in a refined, non-textured microstructure.[50] Capek *et al.*[51] developed porous Zn for implantation into trabecular bone using SPS, achieving a compressive yield strength (∼31 MPa) like that of trabecular bone (1–12 MPa). Based on earlier investigations, various studies have improved the mechanical and biological properties of Zn and its alloys using SPS.[52,53] However, a comprehensive study that examines the microstructural, textural, mechanical, corrosion, and biological behavior of SPS-processed Zn has yet to be reported. To address this research gap, the present investigation aims to thoroughly understand these properties in SPS-processed pure Zn and compare them systematically with cast Zn samples. This comparison will help assess the effectiveness of the SPS process for the fabrication of Zn for biomedical applications.

B. Materials and methods

Commercially pure gas atomized Zn powder with a particle size ranging between 10 μm and 25 μm was used in the present study. A commercially pure Zn block (>99.9%) from Vedanta Ltd. (Mumbai, India) was used in the present study as the cast sample. To achieve microstructural homogenization, cast Zn material was recrystallized at 300 °C for 4 h under ambient conditions. Zn powders were compacted in the form of cylinders of ∼6–7 mm by SPS (HP D10 FCT system, GmbH, Germany) using a graphite die of 20 mm inner diameter. To prevent Zn from sticking with the die and to maintain electrical conductivity during sintering, 0.5 mm thick graphite paper was placed between the graphite punches and the Zn powder. The sintering was performed in a vacuum at 300 °C (temperature) under a uniaxial pressure of 50 MPa. The sintering process involves three distinct stages: initial pressing from 5 MPa to 50 MPa, followed by increasing the temperature from 50 °C to 300 °C at a rate of 50 °C min^{-1} with a dwell time of 10 min; and finally, the cooling stage, where the temperature decreases from 300 °C to 50 °C at the same rate of 50 °C min^{-1}. The structural characterization of the powder and the bulk samples was carried out using a Rigaku Smart Lab X-Ray diffractometer (fitted with Cu-Kα radiation (λ = 1.5406 Å)) between the 2θ range of 30° and 80° with a scan rate and step size of 3° min^{-1} and 0.01°, respectively in Bragg–Brentano mode. The bulk texture of the processed samples was analyzed by using an X-ray goniometer with Schulz reflection geometry (Rigaku Smartlab XRD) and a Cu-Kα source operated at 45 kV and 30 mA on the XY surface.

The microstructural characterization of the samples including optical microscopy (OM) and scanning electron microscopy (SEM) fitted with electron backscattered diffraction (EBSD) was carried out after the samples were subjected to standard metallographic procedures. After mounting the sample, they

are subjected to grinding (sequentially varied up to 4000 μm grit paper) followed by electropolishing and etching. The electropolishing of the samples was performed to obtain a mirror-like surface finish operating under 20 V for 35 s in an electrolyte consisting of orthophosphoric acid and ethanol (3 : 5 ratio). The polished surface was etched for 10 s in 10% nital to characterize the grain morphology using an OM (Leica Microsystem) and SEM (Zeiss Gemini SEM 450) equipped with an EDAX EBSD detector. The room temperature compressive strength of the samples was tested by using an Instron 5567 screw-driven universal testing machine at a strain rate of 10^{-3} s^{-1}. The *in vitro* biodegradation behavior of the samples was assessed by immersing them in simulated body fluid (SBF) for 7, 14, and 21 days, respectively. The SBF solution was prepared according to the method outlined elsewhere but in.[54] Before immersion, all samples were polished using the previously described procedure and subsequently ultrasonicated for 30 min to eliminate any surface contaminants. The samples were then incubated at 37 °C with a 5% CO_2 supply for the specified durations. The mass change was recorded to determine the degradation rate. The electrochemical corrosion behavior of the as-cast and SPS Zn samples was studied using a standard 3-electrode cell setup using a potentiostat (C.H. Instruments, CHI604E, Texas, USA) with standard calomel and platinum (Pt) as the reference and counter electrodes, respectively. Zn samples with an exposure area of 1 cm^2 were used as the working electrode, and simulated body fluid (SBF) was employed as the electrolyte.[55,56] All the samples were mechanically ground up to #4000 grit followed by cloth polishing to obtain scratch-free surfaces of an average roughness of 0.08 μm. The open circuit potential (OCP) for the Zn samples was continuously monitored for 1 h. To understand the corrosion behavior, the samples were covered by the SBF solution for 1 h and 24 h, respectively. After 1 h and 24 h, the electrochemical impedance spectroscopy (EIS) information was recorded. The EIS measurement was performed in the frequency range of 10 kHz to 0.01 Hz by applying 10 mV perturbation to OCP values. Similarly, the potentiodynamic polarization (PDP) tests were carried out for 1 h under the potential range of −0.3 V *vs.* SCE to 0.3 V *vs.* SCE offset to the rest potential with a scan rate of 1 mV s^{-1}. All these studies were repeated three times to ensure repeatability. After PDP and EIS, all the samples were cleaned according to ISO 8407:2009,[33] and the surface morphology of the corroded surface was observed *via* SEM (Model – Zeiss Gemini SEM 450). The corrosion rate (CR) was calculated according to eqn (1).

$$\mathrm{CR} = \frac{I_{\mathrm{corr}} \cdot 1000}{n \cdot F \cdot A} \tag{1}$$

where I_{corr} represents the current density, n denotes the number of electrons (2 in the present case), F signifies the Faraday's constant (96 500 C mol^{-1}), and A stands for the atomic weight of the metal (65.38 g mol^{-1}).

The *in vitro* cytocompatibility of the SPS Zn samples was studied by indirect method by using MC3T3-E1 cells (the MC3T3-E1 preosteoblast cells were obtained from an established commercial supplier, meeting all necessary regulatory and quality standards), and the results were compared with the as-cast Zn samples. Initially disc shaped Zn samples (20 mm diameter and 2 mm thickness) were polished uniformly followed by sterilizing in ethanol and exposed to UV for 1 h. To remove residual ethanol, the samples were further washed thrice using a mixture of phosphate buffer saline solution and 1% antibiotic. Since Zn degrades in the solution media, the effect of leaching out from the material on the cellular response was observed by using conditioned media. Conditioned media was prepared by incubating the sterilized samples in a complete culture medium, *i.e.*, the mixture of α-MEM (minimum essential medium), 10% fetal bovine serum (FBS, Gibco, Life technologies) and 1% antibiotic (Sigma Aldrich) for 24 h and 72 h at 37 °C in the presence of 5% CO_2. A constant amount of 15 μL mm^{-2} of complete media was used to prepare the conditioned media. After the mentioned incubation period, the samples were removed. The conditioned medium was centrifuged (5000 rpm for 20 min) to remove the presence of any debris.

MC3T3-E1 cells were cultured in complete media using a 48-well plate with 3×10^3 cells per well and allowed to attach for 24 h at 37 °C with 5% CO_2. After 24 h of incubation, the media was replaced with a conditioned medium and further incubated for 24 h and 72 h separately. The condition media of the as-cast and SPS Zn were used at two different dilutions: 1× (*i.e.*, 100% conditioned medium) and 8× (*i.e.*, 12.5% concentration of the condition medium and the remaining complete medium). For the positive control, cells were cultured in fresh media and incubated for the same period as that for the conditioned media sample. After the incubation period (1 day and 3 days), the conditioned medium was aspirated, and the cells were rinsed with PBS. Subsequently they were incubated in complete media containing WST-1 (Invitrogen) solution with 1:10 dilution for 3 h to measure the cell viability. The optical density of the resultant medium was analyzed using a plate reader (Biotek Gen 5, Santa Clara, CA, USA) at 440 nm. The cell viability was reported in the form of relative growth rate (RGR), which can be calculated using eqn (2)

$$\mathrm{GR} = \left(\frac{\mathrm{OD}_{\mathrm{sample}}}{\mathrm{OD}_{\mathrm{control}}}\right) \times 100 \tag{2}$$

where $\mathrm{OD}_{\mathrm{sample}}$ and $\mathrm{OD}_{\mathrm{control}}$ are the optical density of the sample, and the control determined with a plate reader. The obtained data from the WST (water-soluble Tetrazolium) assay were subjected to statistical analyses (using standard analytical technique of variance (ANOVA) with Tukey's test). The differences were considered significant at $p < 0.05$. All the data presented are from the results of at least four samples.

The viability of the cells was studied with live/dead assay by staining with Calcein AM (Thermo Fischer Scientific, India) and Ethidium Homodimer dye (Thermo Fischer Scientific, India). This is followed by imaging of the samples using an inverted epi-fluorescence microscope (Olympus IX-53, Tokyo, Japan). The cell morphology was visualized by fixing the cells with 3.7% formaldehyde in PBS solution at room temperature for 30 min, followed by PBS washing. The cell membrane was

permineralized by incubating in a 0.2% Triton X-100 solution (Sigma, Germany) for 8 min at room temperature, followed by PBS washing. The washed cells were incubated with 25 μg mL^{-1} Alexa Fluor 488 (Invitrogen) for 30 min at room temperature for actin staining. The cell nuclei were stained by incubating in 0.2 μg mL^{-1} DAPI (Invitrogen) for 3 min at room temperature. The stained cells were examined using an inverted epi-fluorescence microscope.

C. Results and discussion

C.1 Powder characterization

Fig. 1(a) and (b) depict the SEM images of the Zn powder at different magnifications, showcasing the nearly spherically shaped powder particles with faceted surfaces surrounded by numerous satellites (small particles surrounding the larger ones). The formation of satellites is attributed to the collision between solidifying droplets caused by turbulent flow inside the atomization chamber.[57,58] The particle size distribution plot (shown in Fig. 1(c)) reveals an average powder particle size in the range of 11 ± 6 μm. The X-ray diffraction (XRD) pattern of Zn powder shows the presence of peaks corresponding to the *hcp* (hexagonally closed-packed structure) phase (Fig. 1(d)).

C.2 Sintering and densification

The density of the SPS Zn sample was calculated to be ~7.1 g cc^{-1}, with a relative density of ~99.4%. This indicates that the Zn powder was almost fully densified during the sintering process. According to Abedi *et al.*,[59] in metallic samples, a homogeneous temperature distribution is achieved in all directions, resulting in higher consolidation rates compared to ceramic samples.[60–62] Fig. 2 shows the sintering cycle plot (in terms of piston displacement *vs.* time and temperature *vs.* time). Sintering takes place in distinct stages until final densification of the powders and the sintering

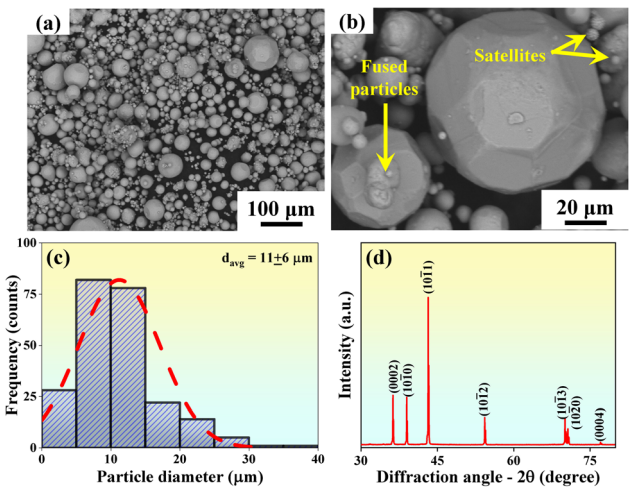

Fig. 1 Scanning electron microscopy images showing the morphology of the Zn powder at (a) lower and (b) higher magnifications. (c) Particle size distribution plot showing the average density of the Zn powders, and (d) X-ray diffraction pattern of the Zn powder showing the presence of the hexagonally closed packed structure.

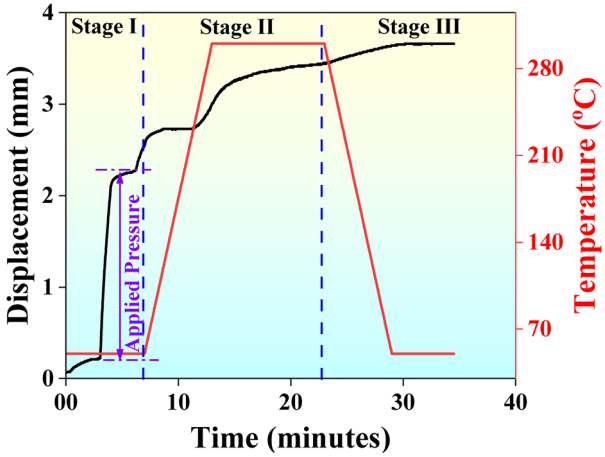

Fig. 2 Plot showing the spark plasma sintering cycles observed due to piston displacement and temperature as a function of time for the Zn samples.

stages are briefly outlined as follows: during stage I, a gradual pressure of 50 MPa was applied to the powder without any increment in temperature. The application of pressure allows the powder particles to rearrange and move closer to each other, leading to a reduction in pore size.

Considerable piston displacement with an average rate of 0.35 mm min^{-1} was observed. In the next stage II, the temperature increased quickly, resulting in the generation of plasma between the powder particles. The particle surface was cleaned, and thermally activated densification takes place.[63] A piston displacement of 0.1 mm min^{-1} was observed during this stage. The temperature changes from 50 °C to 300 °C at the rate of 50 °C min^{-1} with a dwell time of 10 min, which leads to grain boundary diffusion, necking, and pore closure. In the last stage III, the cooling stage, the temperature decreases from 300 °C to 50 °C at a rate of 50 °C min^{-1}. The piston displacement reduces to 0.01 mm min^{-1}, and this piston motion is attributed to the thermal shrinkage of the sample and this shrinkage doesn't play any role in densification.[64]

C.3 Structural characterization

Fig. 3 illustrates the XRD pattern of pure Zn powder and bulk samples. The XRD patterns show the presence of a single-phased microstructure with the peaks corresponding to the *hcp* phase. No additional peaks corresponding to other phases are observed within the deductible limits suggesting that no oxides are formed during sintering. The peak intensity for the powder is observed at (10$\bar{1}$1). On the other hand, the peak intensity is observed at (0002) for the bulk samples. The change in the peak's intensity can be attributed to the preferred orientation, where the crystallites (in a polycrystalline material) align in a specific crystallographic plane during the fabrication process, such as casting, sintering, *etc.*[65–68] During SPS, Zn powder is subjected to high temperature and pressure, and the individual particles start bonding and densifying. During this process, the crystallites may reorient themselves in a specific fashion. Several factors including sintering conditions, particle

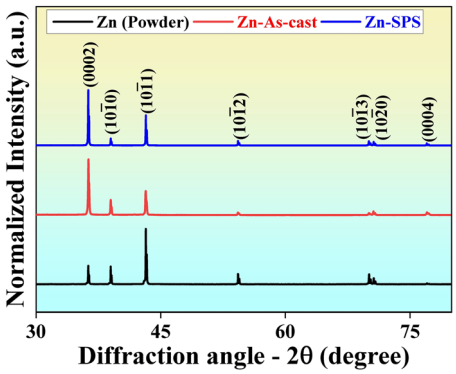

Fig. 3 The X-ray diffraction patterns for the as-received zinc powder and the bulk Zn samples fabricated by both casting and SPS processes.

morphology, mechanical deformation, cooling rate, *etc.*, can affect the preferred orientation during processing. Similarly, during casting, when molten material solidifies into a polycrystalline structure, the cooling rate and solidification conditions can influence the alignment of crystallographic planes within the newly formed grains. In materials with a *hcp* structure, the grains preferred orientation is based on their *c*/*a* ratio, and Zn has a *c*/*a* ratio greater than 1.633. Therefore, the basal plane [0002] is parallel to the surface.[69]

C.4 Bulk texture studies

The X-ray texture goniometer was utilized to measure the bulk texture of both the as-cast and SPS samples. The Schulz reflection method was used to measure the total six pole figures. The basal (0002), prismatic (1010), and (1120) pole figures are shown in Fig. 4. The (0002) pole figure shows the highest misorientation random distribution (MRD) value of ~17 for the cast sample, but it reduces to ~3 for the SPS Zn sample. In the as-cast condition, the (0002) pole figure shows slightly off-basal orientation with other texture components, whereas in the SPS sample, cantered basal orientation with lower intensity is observed. During SPS, the rapid heating and cooling cycle, along with the application of pressure, leads to recrystallization, grain growth, and plastic deformation. These processes tend to disrupt any initial texture present in the starting powder. The uniform orientation achieved during SPS can contribute to a more isotropic microstructure and mechanical properties. The interdependence theory suggests that fine and equiaxed grains obtained due to grain refinement during sintering show a weak texture.[35,70]

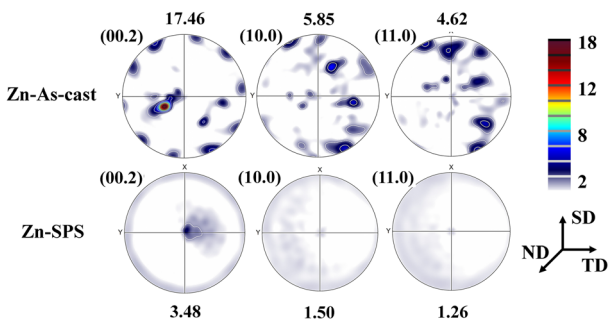

Fig. 4 Pole figures measured by X-ray texture goniometer for the as-cast and spark plasma sintered Zn samples along the following planes: planes (0002), (1010), and (1120).

C.5 Microstructural characterization

The surface morphology of the as-cast and SPS samples was characterized through optical and scanning electron microscopy, and the corresponding images are presented in Fig. 5. A non-uniform microstructure, along with a significant number of twins (yellow arrows), is observed in the as-cast samples (Fig. 5(a) and (b)). Furthermore, some fine grains are observed within the coarse grains (red arrows) in Fig. 5(b), which may be due to recrystallization. Fig. 5(c) and (d) illustrate the microstructure of the SPS Zn samples. The samples were sintered adequately, as there were no visible sintering defects (like cracks and pores at the considered magnification), and thus, the density of the SPS Zn samples should be closer to the theoretical density (ρ = 7.1 g cc^{-1}). Enhanced densification during the SPS process is attributed to the plastic deformation of powder particles and the application of both temperature and pressure during the sintering process. According to Chaim *et al.*,[71] as the applied stress reaches the yield strength, the densification takes place by plastic deformation. Powder particle size significantly influences densification, with larger particles undergoing plastic deformation under external pressure while smaller particles melt and evaporate locally during the process.[72] The microstructure appears to be a regular arrangement of large grains (circular shape) of uniform size.[73] The larger grain may contain some finer grains along with their boundaries considered to be sub-grain boundaries.

The detailed sintering mechanism and the effect of the process parameter on the microstructure can be explained as follows: the applied heating rate of 50 °C min^{-1} during the second stage of sintering (from 50 °C to 300 °C) induces a non-equilibrium condition, promoting the formation of fine recrystallized grains while minimizing the grain growth. Localized Joule

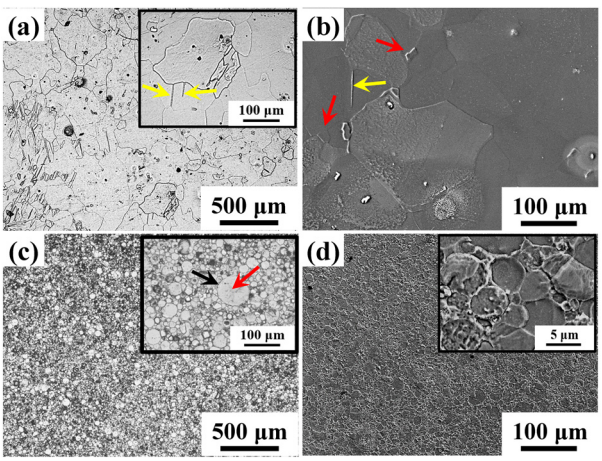

Fig. 5 (a) and (c) Optical and (b) and (d) scanning electron microscopy images of the zinc samples fabricated by (a) and (b) casting and (c) and (d) spark plasma sintering processes.

heating at particle contact points enhances densification by increasing the driving force for diffusion, thereby restricting excessive grain coarsening.[74–77] Moreover, the pulsed DC current in SPS induces localized heating at grain boundaries promoting sintering through grain boundary diffusion, while the short pulse duration effectively limits grain coarsening. This controlled diffusion mechanism leads to the formation of a finer and more uniform grain structure, further enhancing the material's mechanical properties.[78] The application of 50 MPa uniaxial pressure throughout the sintering process facilitates plastic deformation, leading to a significant increase in dislocation density at grain boundaries. This, in turn, activates dynamic recrystallization (DRX), where newly nucleated grains replace deformed ones, resulting in a refined microstructure. Additionally, DRX disrupts the initial texture, contributing to a more isotropic grain orientation.[79] These mechanisms collectively contribute to the superior microstructural characteristics of SPS-processed Zn, distinguishing it from conventionally cast counterparts.

For a better understanding of the crystal orientation and grain boundary characteristics, electron backscatter diffraction (EBSD) analysis was carried out on the Zn samples (Fig. 6). The orientation map developed on the sample surface represents the crystal direction normal to the surface and is referred to as the inverse pole figure (IPF). Most of the grains in the SPS samples are red-colored, suggesting that these grains have their *c*-axes positioned close to the specimen's normal direction, thus indicating that their basal planes {0001} are nearly parallel to the surface. Fig. 6(b) and (e) show the grain boundaries superimposed image quality (IQ) map for the bulk Zn samples. The blue lines in the IQ maps indicate high-angle grain boundaries (HAGBs) with angles exceeding 15°, while red and green lines denote low-angle grain boundaries (LAGBs) characterized by angles below 15°. The as-cast sample displays around 33% LAGBs, while the SPS sample shows ~15% LAGBs. Notably, in the SPS sample, LAGBs primarily appear in sub-grains within coarse grains, while fine grains tend to be relatively free of LAGBs. The SPS samples have smaller grains (~19 μm) compared to the as-cast sample (~150 μm) with more HAGBs. Areas with fine-grain regions show more HAGBs, possibly due to the strained concentration. The transition from LAGBs to HAGBs is believed to occur mainly during dynamic recrystallization, which is triggered by the combination of applied pressure and temperature observed during the SPS process. Hence, a bimodal grain structure characterized by the coexistence of both coarse and fine grains is observed. On the other hand, the as-cast samples exhibit a predominantly coarser grain with pronounced twin formation. These differences in the microstructural characteristics between the as-cast and SPS samples highlight the distinct variations in the processing methods and thermal conditions/variations observed during the respective manufacturing processes. While the SPS process facilitates dynamic recrystallization and grain refinement, the as-cast samples retain a coarse grain structure with evident twin boundaries.

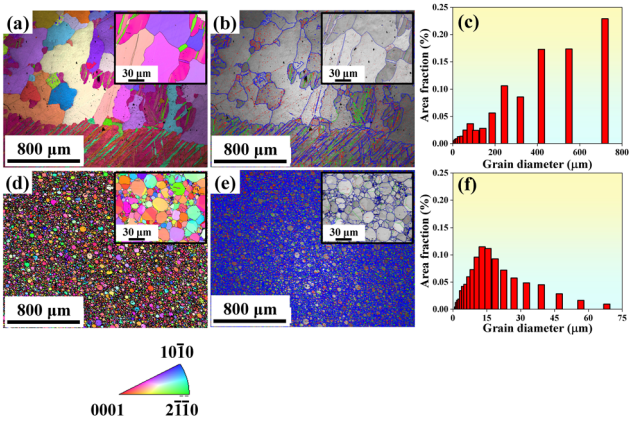

Fig. 6 Electron backscattered diffraction results showing the inverse pole figure (IPF) maps, image quality (IQ) maps, and the grain size distribution plot of the (a)–(c) as-cast and (d)–(f) spark plasma sintered samples, respectively.

C.6 Mechanical testing

Fig. 7 depicts the compressive stress–strain and strain–hardening plots of the as-cast and SPS samples. The yield strength (0.2% PS, YS) observed for the SPS sample was significantly higher (115 ± 4 MPa) than that of the cast sample (60 ± 16 MPa). However, the ultimate compressive strength (UCS) observed for the as-cast sample was found to be in the range of 274 ± 37 MPa, which is higher than that of the SPS samples (191 ± 6 MPa). The increase in the YS of the SPS sample is due to the formation of micron and sub-micron grain during the SPS process. The strengthening mechanism during SPS can also be explained with the help of Hall–Petch equation according to which fine and uniform grains offer higher strength as compared to coarse-grained as-cast samples as explained below:

$$\sigma_{\text{yield}} = \sigma_0 + kd^{-1/2} \quad (3)$$

$$\sigma_{\text{yield}} \propto d^{-1/2} \quad (4)$$

where σ_{yield} is the yield strength of the material, σ_0 is the lattice friction stress, k is the Hall–Petch coefficient, and d is the average grain size of the material. The grain size plays a crucial role in determining the yield strength of materials. Specifically, a finer grain size (~19 μm) enhances yield strength (~115 MPa), whereas a coarser grain structure, such as in cast Zn (~150 μm), results in lower yield strength. This occurs because materials with

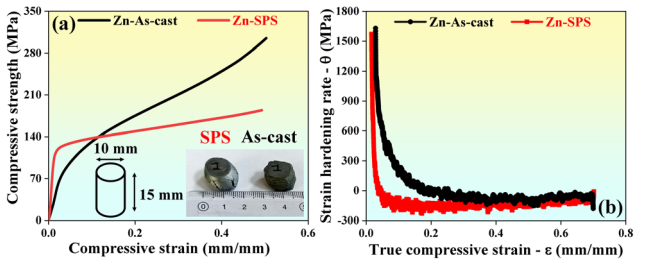

Fig. 7 (a) True compressive stress and strain and (b) strain hardening rate *vs.* strain plots for the bulk Zn samples fabricated by casting and spark plasma sintering.

smaller grains have a higher density of grain boundaries, which impedes dislocation movement and increases the energy required for dislocations to move into adjacent grains. As a result, the yield strength of SPS samples is higher than that of the cast samples. However, the trend is reversed for ultimate compressive strength; SPS samples exhibit lower strength (~191 MPa), whereas cast samples demonstrate higher strength (~274 MPa). This is because grain boundaries, while restricting dislocation motion, also serve as weak points where cracks initiate, leading to brittle fracture before significant plastic deformation can occur. In hexagonal close-packed (HCP) materials, deformation occurs through a combination of dislocation slip and twinning. In as-cast Zn samples, the presence of larger grains and strong basal texture (as discussed in Section 3.4) facilitates twinning as a dominant deformation mechanism. Twinning allows additional strain accommodation at higher stress levels, leading to an increase in ultimate compressive strength (UCS).[80] During SPS, recrystallization restricts the twin formation due to the large obstructive effect of grain boundary on the twinning shear.[81] As a result, deformation is primarily accommodated by dislocation slip, which enhances yield strength but limits strain-hardening mechanisms, leading to a lower UCS compared to that for the cast Zn.

Under the SPS condition, the deformed sample showed uniform bulging, whereas in the as-cast condition, irregular deformation is observed (Fig. 7(a) inset). Bulging generally refers to increased absorption of energy due to uniform deformation of load with less twin activity. Fig. 7(b) shows the strain hardening rate (θ) *vs.* true strain behavior under compression. In the SPS sample, the strain hardening rate decreases rapidly with increasing strain, whereas in the as-cast condition, it reaches the plateau. The extended strain hardening behavior in the as-cast sample might be due to the presence of the coarse-grained microstructure and the formation of twins. Table 1 summarizes the mechanical properties of SPS Zn, along with a comparison to previously reported studies on pure Zn and its alloys fabricated using various manufacturing methods.

C.7 Immersion study and electrochemical behavior

C.7.1 Immersion study. The immersion behaviors of the as-cast and SPS samples were analyzed according to ASTM G31-72 standards, where polished Zn samples were immersed in simulated body fluid (SBF) under simulated physiological conditions for 7, 14, and 21 days. During the initial 7 days of immersion, a thin, uniform whitish layer formed on the SPS Zn surface. As the immersion time increased, this layer gradually thickened, and degradation products began to accumulate unevenly, as shown in Fig. 8. After 7 days, the degradation rate of the SPS Zn sample was 0.1325 mm per year, which is consistent with previously reported values.[82] At extended immersion periods of 14 and 21 days, the degradation rates further decreased to 0.0965 mm per year and 0.075 mm per year, respectively. This gradual reduction in degradation rate is attributed to the formation of a thicker protective layer, which acts as a barrier, limiting ion exchange between the sample surface and the surrounding medium. However, in the initial stages, the weaker and unstable oxide layer undergoes continuous breakdown, leading to surface void formation and progressive degradation.

The degradation mechanism of Zn in SBF can be explained as: during the initial stages of electrochemical corrosion, upon exposure to simulated body fluid (SBF), Zn begins to dissolve, initiating oxygen reduction at the cathode according to the following anodic and cathodic reactions (5) and (6):

$$Zn \rightarrow Zn^{2+} + 2e^{-} \quad (5)$$

Table 1 A comparison of the mechanical properties of pure zinc and zinc-based alloys/composites fabricated using different fabrication techniques. MR represents the manufacturing route employed, GM – grain morphology, ρ – density, H – hardness, YS – yield strength in compressive mode unless mentioned as tensile mode, US – ultimate strength in compressive mode unless mentioned as tensile mode, E – elastic modulus (GPa), and Ref. – reference article

Material designation	MR	GM		ρ/porosity	H	YS (MPa)	US (MPa)	E (GPa)	Ref.
		Size (μm)	Shape						
Pure Zn	WAAM	14 ± 5	Equiaxed	—	35 ± 2 $HV_{0.3}$	—	—	—	89
	Wrought	11 ± 4	—	—	41 ± 1 $HV_{0.3}$	—	—	—	
Ti–5Zn	Hot Pressing	—	—	—	158 ± 18 HV	651 ± 3	—	17 ± 2	90
Ti–10Zn		—	—	—	—	934 ± 32	—	20 ± 2	
Ti–20Zn		—	—	—	390 ± 43 HV	1136 ± 10	—	27 ± 2	
Ti–30Zn		—	—	—	270 ± 35 HV	—	—	4 ± 1	
Zn-16HAp (wt%)	SPS	—	—	18%	24 ± 5 HV_5	46 ± 3 (Tensile)	65 ± 4 (Tensile)	—	53
CP Zn		—	—	20 ± 2%	29 $HV_{0.3}$	43 ± 2	—	—	51
FP Zn		—	—	21 ± 2%	17 $HV_{0.3}$	31 ± 5	—	—	91
Zn		—	—	—	43 ± 2	53 ± 17	171 ± 13	—	
Zn-5Ge	Cast	—	—	—	38 ± 0.6 $HV_{0.1}$	29 ± 3 (Tensile)	34 ± 6 (Tensile)	—	92
	Hot rolled	—	—	—	39 ± 1 $HV_{0.1}$	84 ± 3	153 ± 3	—	
Pure Zn	Cast	150	Coarse	7 g cc^{-1}	—	60 ± 16	274 ± 37	—	Present
	SPS	19	Fine/equiaxed	7.1 g cc^{-1}	—	115 ± 4	191 ± 6	—	work
Human cortical bone	—	—	—	5–10%	—	80–120	—	3–30	93

WAAM – wire arc additive manufacturing; Hap – hydroxyapatite; SPS – spark plasma sintering; CP – coarse powder (600–850 μm); FP – fine powder (40–100 μm).

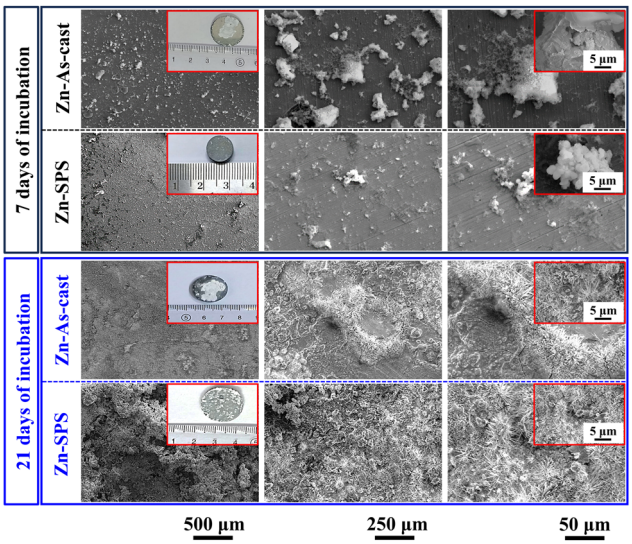

Fig. 8 Scanning electron microscopy images of the spark plasma sintered Zn samples after 7 days and 21 days of immersion in simulated body fluid (SBF). The insets show macroscopic views and high-magnification images. After 7 days of immersion, a thin corrosion layer forms with localized deposits, while after 21 days, a thicker, more uniform degradation layer develops, indicating surface stabilization.

$$O_2 + 2H_2O + 4e^- \rightarrow 4OH^- \quad (6)$$

The by-product OH^- of the cathodic reaction increases the pH value, according to the Pourbaix diagram;[83] as the pH of the electrolyte increases, zinc ion (Zn^{2+}) reacts with the hydroxide (OH^-) ion by dehydration reaction to form $Zn(OH)_2$, which further transforms into a thermodynamically stable zinc oxide (ZnO) layer according to reaction (7) and (8):

$$Zn^{2+} + 2OH^- \rightarrow Zn(OH)_2 \quad (7)$$

$$Zn(OH)_2 \rightarrow ZnO + H_2O \quad (8)$$

However, the zinc oxide layer tends to dissolve back into Zn^{2+} due to the leaching action of aggressive Cl− competing with the surface hydroxyl groups in $Zn(OH)_2$ according to reaction (9), resulting in the formation of $ZnCl_2$:

$$Zn(OH)_2 + 2Cl^- \rightarrow Zn^{2+} + 2OH^- + 2Cl^- \quad (9)$$

After 24 h of incubation, a thick corrosion product forms on the sample's surface. The change in surface morphology probably influenced both mass transport and the ionic diffusion. Thus, the corrosion mode varies, and the degradation of pure Zn accelerates progressively with the co-existence of calcium (Ca^{2+}) and phosphate (PO_4^{3-}) ions, leading to the formation of calcium phosphate precipitates according to reactions (10)–(12).[84] A schematic representation of the corrosion mechanism of pure Zn immersed in a simulated body fluid solution is shown in Fig. 9.

$$5Zn(OH)_2 + 2HCO_3^- + 2H^+ \rightarrow Zn_5(CO_3)_2(OH)_6 + 4H_2O \quad (10)$$

$$3Ca^{2+} + 2PO_4^{3-} \rightarrow Ca_3(PO_4)_2 \quad (11)$$

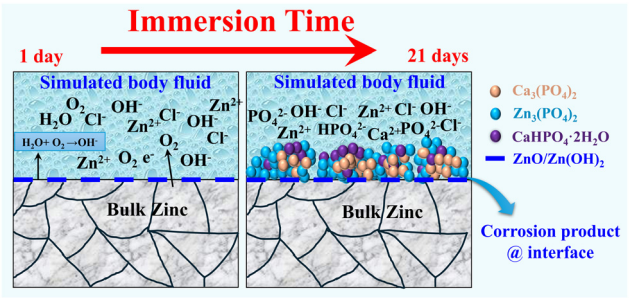

Fig. 9 Schematics illustrating the corrosion mechanism in pure Zn immersed in simulated body fluid for long term degradation studies.

$$Ca^{2+} + HPO_2^{4-} + 2H_2O \rightarrow CaHPO_4{\cdot}2H_2O \quad (12)$$

C.7.2 Open circuit potential studies. The bulk Zn samples fabricated by casting and SPS were immersed for 1 h in simulated body fluid (SBF) to examine the potential variation in terms of OCP. From Fig. 10, it is evident that there is a decrease in potential (E_{OCP}) upon initial immersion in the solution and the potential stabilizes between 1400 to 1800 s for both the sample conditions. The SPS Zn sample demonstrated a final OCP value of −1.03 V, which is slightly more active than the as-cast Zn sample (−1.02 V). The active behavior of both samples could be attributed to the deposition of corrosion products in the SBF media and the dissolution of the corrosion film developed on the sample surface.[85] The variation in the OCP stabilization between the as-cast and SPS Zn samples is mainly due to the microstructural variations among the samples as already discussed in Section 3.5. The refined grain structure of the SPS Zn, with increased grain boundary area, accelerates the initial surface reactions, leading to rapid passivation and earlier stabilization of the OCP.[86,87] Additionally, the disruption of the initial texture, potentially enhances the uniformity and stability of the passive film.[88]

This, in turn, promotes a more stable electrochemical response compared to as-cast Zn. The formation and stability of surface corrosion products further influence the OCP

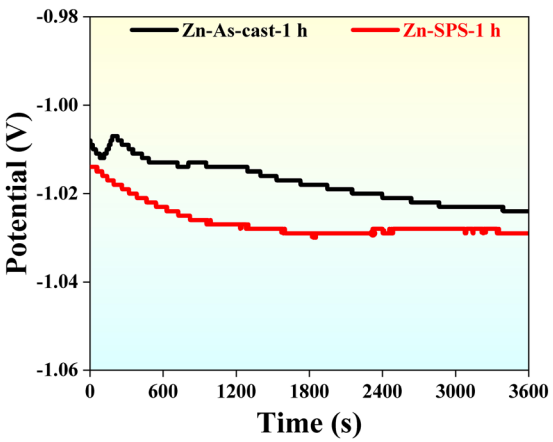

Fig. 10 Open-circuit potential (OCP) behavior of Zn as-cast and SPS samples for an exposure period of 1 h in SBF.

Table 2 Table furnishing the polarization data for the as-cast and SPS zinc samples immersed in simulated body fluid environments

Sample condition	E_{corr} (V) *vs.* SCE	I_{corr} (μA cm^{-2})	I_p (μA cm^{-2})	E_{pp} (V) *vs.* SCE	E_{pb} (V) *vs.* SCE	CR (mm per year) × 10^{-4}
As-cast	−1.21 ± 0.02	8.61 ± 0.11	62.0 ± 3.1	−1.16 ± 0.03	−1.06 ± 0.17	0.60 ± 0.08
SPS	−1.20 ± 0.04	12.16 ± 0.90	52.9 ± 1.2	−1.15 ± 0.03	−1.03 ± 0.23	0.88 ± 0.05

behavior, as the SPS Zn surface tends to form a more homogenous and protective oxide layer at an early stage of immersion (Table 2).

C.7.3 Potentiodynamic polarization studies. Fig. 11 illustrates the potentiodynamic polarization (PDP) curves for the Zn samples (fabricated by casting and SPS). The corrosion parameters such as corrosion current (I_{corr}), and corrosion potential (E_{corr}) were analyzed *via* the Tafel extrapolation method,[94–96] and the values are tabulated in Table 2. The E_{corr} values of both the as-cast and SPS Zn samples are similar, but the values become significantly active when compared to the OCP values since the Tafel measurements were conducted after the OCP measurements. During the OCP measurements, no external current was supplied, and the equilibrium values were recorded. However, during the Tafel measurements, the samples were already exposed to the SBF environment. In this environment, Zn reacted with Cl, leading to degradation and resulting in a lower potential.

The anodic branch of the Zn samples shows an active-to-passive transition in SBF. Initially, these samples undergo typical active anodic dissolution, followed by passivation at higher potentials. Due to the formation of a passive film, the current density remains constant during the passive region (as seen in Fig. 11). However, after breakdown potential (E_{pb}), the current increases significantly, indicating transpassive corrosion. From the Tafel curve, the corresponding values of I_{corr}, E_{corr}, I_p (passivation current density), E_{pp} (passivation potential), E_{bp} (breakdown potential), and corrosion rate (CR) are calculated and are tabulated in Table 2. The Tafel extrapolation data show that both the as-cast and SPS zinc samples exhibit a similar trend in the cathodic region, with E_{corr} observed to be −1.21 and −1.20 V and I_{corr} measured at 8.61 and 12.16 μA cm^{-2}, respectively. Upon increasing the potential, a stable oxide layer forms, indicating the passive regime. The passivation potential (E_{ap}) was recorded as −1.16 and −1.15 V for the as-cast and SPS samples, respectively. The passivation current density (I_p) was recorded as 62.0 and 52.9 μA cm^{-2} for as-cast and SPS samples, respectively. The stable passivation current in this regime suggests the formation of a passivation layer with a lower I_p indicating better corrosion resistance. Furthermore, the current starts to increase in both samples at the breakdown of the passive layer. The breakdown potentials (E_{pb}) for the as-cast and SPS samples are observed to be −1.06 and −1.03 V, respectively.

Such differences in potential likely arise from the grain size differences (a smaller grain size of 19 μm is observed for the SPS Zn sample leading to a higher density of grain boundaries per unit volume, contrasting with the larger grain size of 150 μm observed in the as-cast condition). The grain boundaries, due to their elevated energy state and altered chemical composition, are inherently more susceptible to corrosion than the bulk material. Furthermore, the presence of fine grains facilitates higher hydrophilicity,[97] increased diffusion, and deeper penetration into the material, potentially leading to localized pitting, as evident from SEM micrographs (Fig. 12). Additionally,

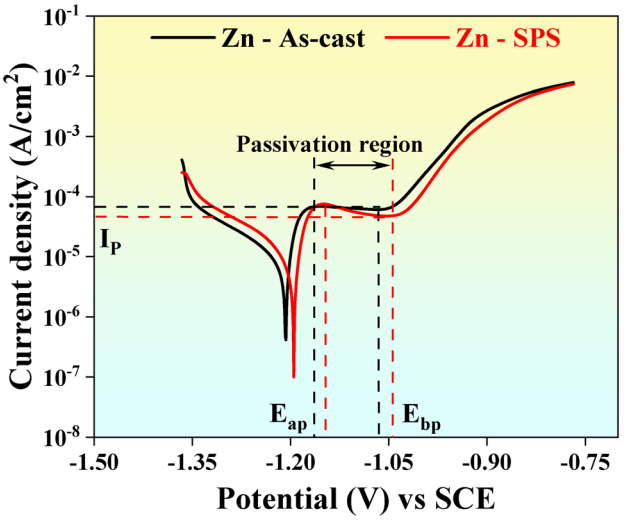

Fig. 11 Potentiodynamic polarization curves obtained after immersion in simulated body fluid for 1 h.

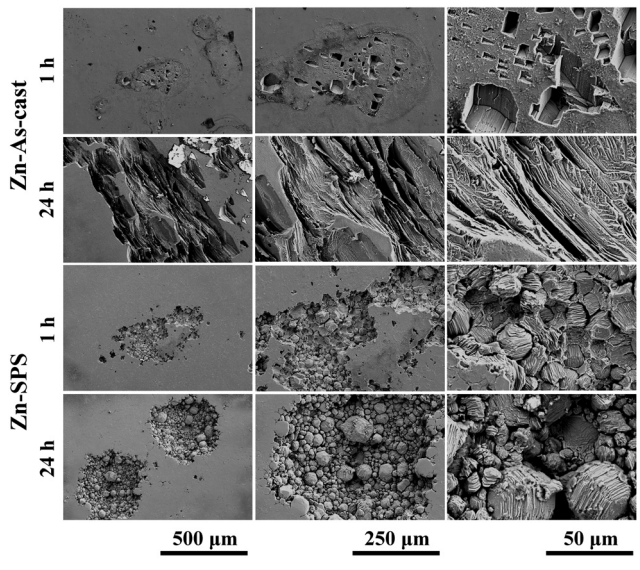

Fig. 12 Scanning electron microscopy images showing the microstructure of the zinc samples after potentiodynamic polarization immersion in simulated body fluid.

Table 3 The polarization data for the as-cast and SPS zinc samples immersed in simulated body fluid as a function of time, compared with other published reports

Material	Manufacturing route	Electrolyte	Degradation parameter				Ref.
			Corrosion rate (mm per year)	Immersion time (days)	I_{corr} (μA cm^{-2})	E_{corr} (V) *vs.* SCE	
Pure Zn	Extrusion	SBF	0.048	56	3.241	−1.033	85
		SBF + Gln	0.023		4.135	−1.055	
		SBF + Glucose	0.014		5.675	−1.099	
		SBF (Tris-HCl)	0.033		4.119	−1.024	
		SBF (Tris-HCl) + Gln	0.034		2.951	−1.004	
		SBF (Tris-HCl) + Glucose	0.027		4.815	−0.999	
Pure Zn	Wrought	SBF	0.30 ± 0.10	—	6 ± 1	−1.13 ± 0.16	98
Pure Zn	WAAM		0.45 ± 0.20	—	9 ± 1	−1.18 ± 0.03	
Zn–1Mg	Cast		—	—	1.2	−0.98	99
Zn–1.5Mg			—	—	8.8	−0.93	
Zn–3Mg			—	—	7.4	−0.93	
Mg–0.5Zn	Cast	SBF	—	—	131 ± 6	−1.87 ± 0.01	100
Mg–1Zn			—	—	124 ± 10	−1.83 ± 0.01	
Mg–2Zn			—	—	115 ± 10	−1.81 ± 0.02	
Mg–3Zn			—	—	102 ± 8	−1.71 ± 0.04	
Ti–5Zn	Hot press sintering	SBF	—	—	0.692	−0.187	101
Ti–10Zn			—	—	0.975	−0.202	
Ti–20Zn			—	—	0.741	−0.178	
Ti–30Zn			—	—	3.631	−0.245	
CP Zn	SPS	SBF	0.61 ± 0.11	14	—	—	102
FP Zn			0.75 ± 0.12		—	—	
Zn16HAp	SPS	SBF	0.41	14	—	—	103
Zn-0HAp	SPS	Hank solution	0.073 ± 0.042	1.5 h	4.90 ± 2.810	−0.942 ± 0.07	104
Zn-1HAp			0.327 ± 0.050		21.07 ± 3.25	−1.281 ± 0.03	
Zn-5HAp			0.630 ± 0.011		39.12 ± 0.66	−1.274 ± 0.01	
Zn-10HAp			0.856 ± 0.031		51.04 ± 1.80	−1.290 ± 0.01	
Pure Zn	As-cast	SBF	0.0179 ± 0.002	1 h	9.43 ± 0.11	−1.21	Present work
			0.0017 ± 0.002	24 h	8.73 ± 0.42	−1.09	
	SPS		0.0025 ± 0.001	1 h	12.93 ± 0.9	−1.2	
			0.0016 ± 0.002	24 h	8.43 ± 0.27	−1.07	

WAAM – wire arc additive manufacturing; SBF – simulated body fluid; Gln – glutamine.

it is worth noting that the texture of the samples also plays a significant role in influencing their corrosion behavior.[88] As discussed above, Fig. 11 indicates the stable passivation layer between −1.15 V to −1.05 V in both the as-cast and SPS Zn samples; beyond that, both the samples indicate the dissolution of the passive layer and the inner material is directly exposed to the corrosive environment increasing the corrosion rate. As indicated above, with a decrease in grain size, an increase in corrosion rate was observed for the SPS sample. This disparity suggests a lower corrosion rate (CR) attributed to the formation of a stable oxide layer, as depicted in Table 2, and the corrosion results of the present work with previously reported work are compared in Table 3.

Fig. 12 shows the SEM images and Fig. 13 shows the EDS images of the corroded Zn samples after 1 h and 24 h immersion time in SBF. The samples, after 1 h of polarization, show the localized form of corrosion with different pit sizes. The as-cast sample shows many pits of the uniform cross-section in a concentrated region/area; however, in the case of the SPS sample the corroded region spreads uniformly with the formation of deep grooves inside the pits (see the higher magnification image in Fig. 12) due to the larger density of grain boundaries. The SEM images reveal that the dissolution is more pronounced at grain boundaries, likely due to their higher activity at these boundaries. The regions adjacent to grain boundaries form micro-level galvanic couples, facilitating

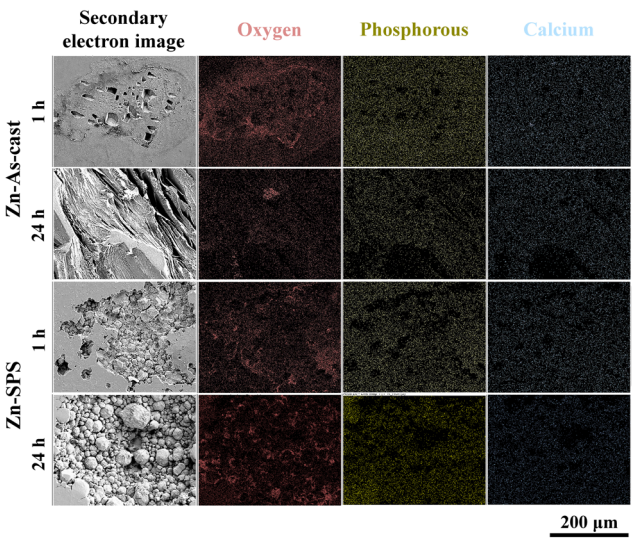

Fig. 13 Energy dispersive spectroscopy images showing the microstructure of the zinc samples after potentiodynamic polarization immersion in simulated body fluid.

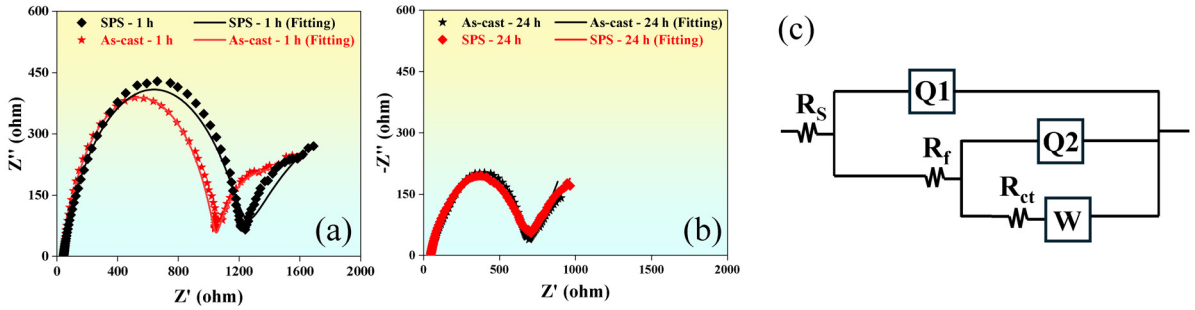

Fig. 14 Plots showing the electrochemical impedance spectroscopy (EIS) result of both the as-cast and SPS zinc samples: Nyquist plots of impedance spectra obtained after (a) 1 h and (b) 24 h of study in SBFs along with (c) the equivalent electrical circuit used to fit the EIS data using Zsimp software.

increased electron transfer and making them more susceptible to activation and localized corrosion.

Both the as-cast and SPS samples display similar electrochemical corrosion behavior but differ in corrosion morphology, likely due to the differences in their microstructural feature (mainly grain morphology), where finer grains are observed in the SPS samples compared to their as-cast counterparts.

C.7.4 Electrochemical impedance spectroscopy. Fig. 14 shows the electrochemical impedance spectroscopy (EIS) results of Zn samples immersed in SBF for 1 h and 24 h. From Fig. 14(a) and (b), all the Nyquist plots exhibited multiple arcs. Furthermore, the impedance response of the Zn samples after 1 h of immersion (Fig. 14(a)) exhibits a semi-circular loop in the high-frequency region followed by a circular arc in the low-frequency region and a straight line with a slope close to 1. Relatively, the impedance of samples after 24 h of immersion (Fig. 14(b)) shows a similar pattern with a varied degree of reaction resistance between the electrolyte and electrode interface. To analyze and fit the electrochemical data, an equivalent electrical circuit model consisting of $[R_s(Q_1(R_f(Q_2[R_{ct}W])))]$ is considered (Fig. 14(c)), where R_s represents the solution resistance, R_f and Q_1 denote the resistance due to the formation of the corrosion product film and the constant phase element for non-ideal capacitance induced by the corrosion product film respectively, R_{ct} is the resistance charge transfer, W represents the Warburg impedance, and Q_2 denotes the constant phase element for non-ideal capacitance induced by the double electrode layer. The values of Q and W can be calculated by using eqn (13) and (14):

$$Q = Y_0^{-1}(j\omega)^{-n} \quad (13)$$

$$W = Y_0^{-1}(j\omega)^{-0.5} \quad (14)$$

where Y_0 is a constant with units of Ω^{-1} S^n for Q and Ω^{-1} $S^{0.5}$ for W, Q is used to obtain a better fit of experimental data, and based on the value of n (−1, 0, and 1), it can be treated as the capacitance, resistance, and inductance respectively, ω is the angular frequency, and the j is the imaginary number equal to $\sqrt{-1}$.

According to Huang *et al.*,[105] the corrosion product covering the sample surface changes the surface condition of the electrode and acts as a time constant. Due to the formation of corrosion product (film) on the sample surface, resistance is induced, which effectively impedes the diffusion of ions during the electrochemical process, leading to the development of Warburg impedance.[105] A similar circuit was also used by Huang *et al.*[105] to study the early electrochemical characteristics of pure Zn in SBF. The fitted parameters obtained are shown in Table 4, where the solution resistance (R_s) value of the electrolyte is observed to be the same for all the samples. However, the R_f and R_{ct} values are very high (1008 Ω cm^2 and 790 Ω cm^2, respectively, for the as-cast samples and 1180 Ω cm^2 and 889 Ω cm^2, respectively, for the SPS samples) during the first hour of the experiment, but these values decrease significantly after 24 h. Subsequently, the R_f and R_{ct} values reach 600 Ω cm^2 and 653 Ω cm^2, respectively, for the as-cast and 658 Ω cm^2 and 257 Ω cm^2, respectively, for the SPS Zn samples. The sharp decrease in R_f and R_{ct} values indicates a significant decline in the protective effectiveness of the corrosion product film and the bare metal surface, respectively.

C.8 *In vitro* bioactivity

Biological analysis is one of the important aspects of the Zn-based biomaterial as it degrades in a biological environment. In this study the cellular response to Zn was assessed by an indirect method wherein the response of cells to the leached degradation products was studied.

C.8.1 Cytocompatibility. The cytocompatibility of the Zn samples was evaluated by incubating cells in a conditioned

Table 4 Equivalent electrical circuit parameters of the as-cast and SPS zinc samples immersed in the simulated body fluid for 1 h and 24 h, respectively

Sample condition	R_s Ω_{cm^2}	R_f Ω_{cm^2}	R_{ct} Ω_{cm^2}	CPE$_1$ (Q_1) $\mu\Omega^{-1}$ cm^{-2} S^n	CPE$_1$ (n_1)	CPE$_2$ (Q_2) $\mu\Omega^{-1}$ cm^{-2} S^n	CPE$_2$ (n_2)	W $\mu\Omega^{-1}$ cm^{-2} $S^{0.5}$	Error (%)
Zn (as-cast)-1 h	40.39	1008	789.6	2.19×10^{-9}	0.8	2.5×10^{-3}	0.8	0.013	5.8
Zn (SPS)-1 h	41.96	1180	889	7.62×10^{-6}	0.76	6.6×10^{-4}	0.8	0.005	7.9
Zn (as-cast)-24 h	40.68	600	653	7.9×10^{-8}	0.8	2.4×10^{-5}	0.6	0.015	2.8
Zn (SPS)-24 h	42.13	658	257	1.94×10^{-5}	0.6	8.02×10^{-3}	0.72	0.017	7.5

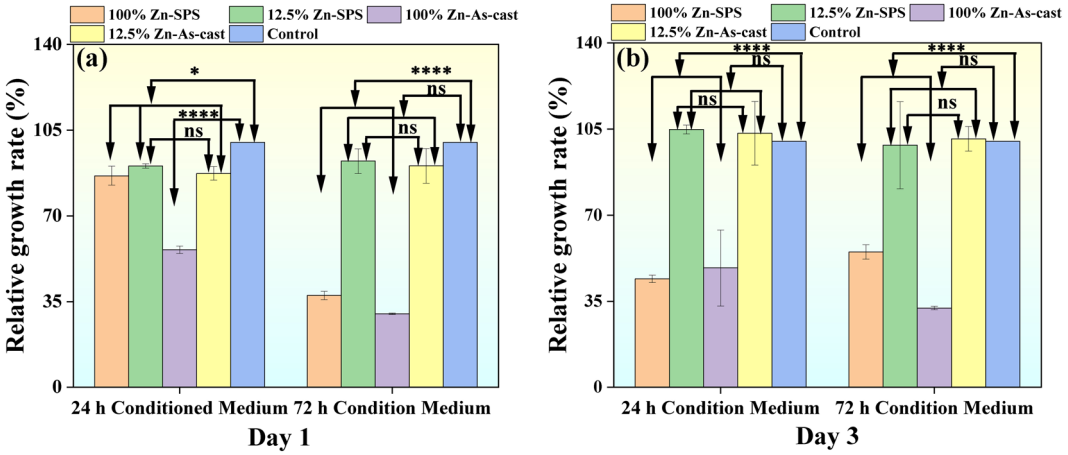

Fig. 15 Relative growth rate measured by WST assay for MC3T3-E1 cells cultured in 24 h and 72 h conditioned media for (a) 1 day and (b) 3 days. The significance level is taken as $p = 0.05$, *i.e.*, $p < 0.05$(*), $p < 0.01$ (*), $p < 0.001$ (*), $p < 0.0001$ (*) and $p > 0.05$, non-significant (ns), $n = 4$.

medium (indirect method). The growth of MC3T3-E1 pre-osteoblast cells was examined in terms of percentage relative growth rate after incubation in the conditioned medium for 1 day or 3 days, with fresh medium serving as the control. The viability of cells cultured in 1× and 8× extracts (100% and 12.5% concentration of conditioned medium) for 1 day and 3 days is depicted in Fig. 15. Fig. 15(a) illustrates the proliferation rate of cells in 24 h and 72 h conditioned media incubated for 1 day. Following an 8-fold dilution, no toxicity was detected, and the growth rates of both samples exhibited comparable results.[106] However, the response of cells in the 72 h conditioned media varies, demonstrating lower compatibility in the 100% extract. Conversely, the response of cells in the 8-fold dilution was favorable. Fig. 15(b) depicts cell proliferation after 3 days of incubation. The relative growth rate in 100% extract for both 24 h and 72 h conditioned media exhibited a significant decrease. However, for the 8-fold diluted conditioned media, no toxicity was observed, and the growth rate was comparable to that of the control for both 24 h and 72 h conditioned media.

A live–dead assay was performed to further evaluate toxicity induced by the leachates from samples. Fig. 16 depicts the live–dead assay result, showing live cells in green color and dead cells in red color. 8-Fold dilution of both the samples showed a minimal number of dead cells for both day 1 and day 3 compared to live cells, confirming the cytocompatibility. It also depicts an increased number of cells on day 3 compared to day 1 in both samples confirming cell proliferation. In the case of 100% extract-conditioned media samples, most of the cells were detached after death, which agrees with the WST assay results. Cellular morphology was characterized by using fluorescence microscopy. Micrographs after day 1 and day 3 of incubation in conditioned media are shown in Fig. 17, where a well-developed cellular morphology with uniformly distributed active fibers is seen

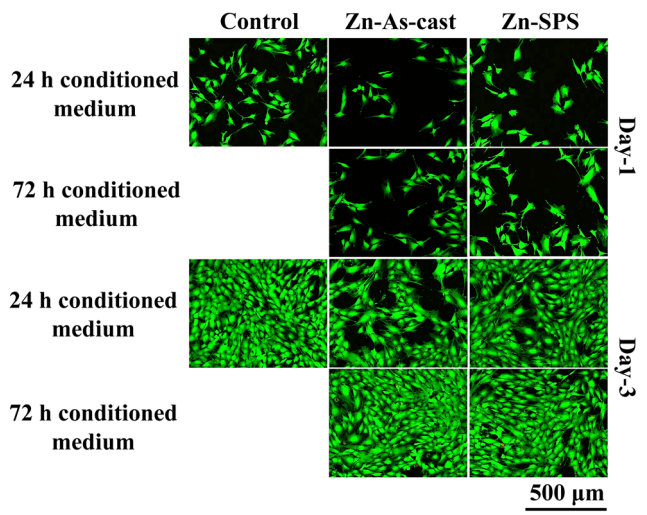

Fig. 16 Representative live/dead stained images of MC3T3-E1 cells treated with conditioned medium (8×) of the as-cast and SPS samples for day 1 and 3 where the live cells are depicted in green while dead cells are depicted in red. Cells cultured in fresh complete media act as the control.

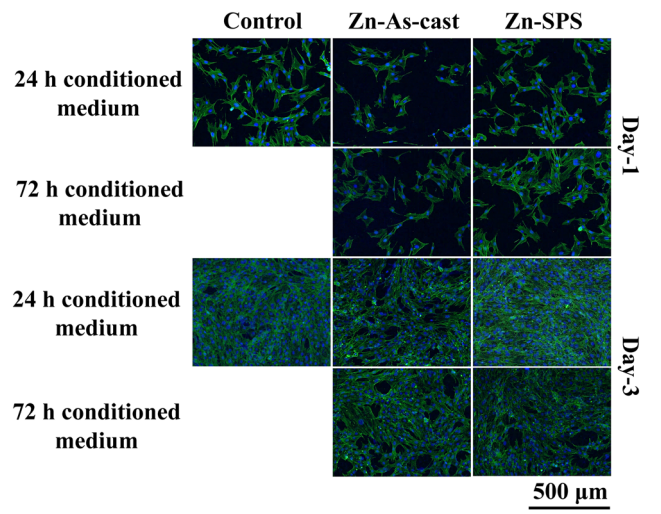

Fig. 17 Representative fluorescent images of MC3T3 cells treated with condition media at day 1 and 3 showing the actin filaments (green) and nuclei (blue) (control represents cell treated with fresh media).

when exposed to 8-fold conditioned media. In both samples, the cellular morphology exhibits good spreading and appears like that of the control samples, which further corroborates the nontoxicity of the 8-fold dilution condition in both samples. In the case of the 100% conditioned samples (both cases), they showed hampered/stressed morphologies. Based on the above study it can be concluded that both the samples exhibited similar and favorable cytocompatibility. At 8-fold dilution, no toxicity was observed, with healthy cell proliferation and morphology comparable to the control. In contrast, 100% of extract-conditioned media showed reduced viability and stressed morphology. These findings confirm that both SPS and as-cast Zn samples exhibit favorable biocompatibility under 8× dilution, making them suitable for potential biomedical applications.

D. Conclusion

The present study systematically compared the microstructural, mechanical, corrosion, and biological properties of SPS-processed Zn with its cast counterpart. Based on this systematic investigation, the following main conclusions are drawn:

• SPS samples have much lower MRD values than their as-cast counterparts. The (0002) pole figure MRD drops from ∼17 in the as-cast sample to ∼3 for the SPS condition due to rapid heating, cooling, and pressure, causing recrystallization and grain growth.

• EBSD analysis reveals that the SPS samples have an average grain size of 19 μm, much smaller than that of the as-cast samples.

• The compressive yield strength of the SPS Zn samples notably increased to 115 MPa compared to the as-cast samples.

• Electrochemical analysis and long-term immersion studies collectively demonstrate that SPS Zn exhibits controlled and gradual degradation in simulated body fluid, similar to that of the cast-Zn. In addition, the formation of a stable and protective corrosion product layer is exhibited, supporting its suitability for biodegradable implant applications.

• The SPS samples exhibit cell viability and proliferation that are like their as-cast Zn counterparts. When exposed to leachates at a dilute concentration (8× dilution of conditioned media), the MC3T3 cells exhibited cell viability that was like that of fresh medium but lower viability for undiluted conditioned media.

• Cytocompatibility studies confirmed that both SPS and cast Zn support cell viability and proliferation, particularly at diluted concentrations.

• Given its refined microstructure, enhanced mechanical performance, and stable degradation behavior, SPS Zn emerges as a promising candidate for biomedical applications, particularly in tissue engineering and biodegradable implant development.

Author contributions

Conceptualization – MKY, JJ, KGP; methodology – MKY, RHS, PK, SN, CSP, PS, JJ, KGP; formal analysis – MKY, RHS, PK, SN, CSP; Investigation – MKY, RHS, PK, SN, CSP, PS; resource – KC, SS, JJ, KGP; writing – original draft preparation – MKY, RHS, PK, SN, CSP, PS; writing – review and editing – MKY, KC, SS, JJ, KGP; supervision – KC, SS, JJ, KGP; project administration – KGP; funding acquisition – KC, SS, KGP.

Data availability

Data may be made available upon reasonable request to the authors.

Conflicts of interest

The authors declare no potential conflicts of interest.

Acknowledgements

The author acknowledges the program for overseas high-level talent's introduction of Henan Province: HNGD2025040 for the financial support.

References

1 J. C. C. Paiva, L. Oliveira, M. F. Vaz and S. Costa-de-Oliveira, *Bioengineering*, 2022, **9**, 409.
2 M. Prakasam, J. Locs, K. Salma-Ancane, D. Loca, A. Largeteau and L. Berzina-Cimdina, *J. Funct. Biomater.*, 2017, **8**, 44.
3 Z. Morsada, M. M. Hossain, M. T. Islam, M. A. Mobin and S. Saha, Appl, *Mater. Today*, 2021, **25**, 101257.
4 V. P. M. Rabeeh and T. Hanas, *Progress in Biomaterials*, 2022, **11**, 163–191.
5 L. Kong, Z. Heydari, G. H. Lami, A. Saberi, M. S. Baltatu and P. Vizureanu, *Materials*, 2023, **16**, 4797.
6 K. Chen, X. Gu and Y. Zheng, *Smart Mater. Manuf.*, 2024, **2**, 100042.
7 K. Chen, X. Gu and Y. Zheng, *Smart Mater. Manuf.*, 2024, **2**, 100042.
8 B. Hutchinson, J. Komenda, S. Kada, M. Barnett and A. Oskarsson, *Scr. Mater.*, 2019, **166**, 78–80.
9 I. D. Engler, P.-A. Hart, D. P. Swanson, J. M. Kirsch, J. P. Murphy, M. A. Wright, A. Murthi and A. Jawa, *Semin. Arthroplasty*, 2022, **32**, 751–756, DOI: **10.1053/J.SART.2022.07.001**.
10 M. I. Z. Ridzwan, S. Shuib, A. Y. Hassan, A. A. Shokri and M. N. Mohammad Ibrahim, *J. Med. Sci.*, 2007, **7**, 460–467, DOI: **10.3923/jms.2007.460.467**preprint.
11 I. Bendich, C. M. Lawrie, V. Riegler, R. L. Barrack and R. M. Nunley, *J. Arthroplasty*, 2022, **37**, S221–S225.
12 K. Praveenkumar, J. Vishnu, A. Raheem, V. Gopal, S. Swaroop, S. Suwas, B. Shankar and G. Manivasagam, *Appl. Surf. Sci.*, 2024, **665**, 160334.
13 R. Shukla and K. G. Prashanth, *Trans. Indian Inst. Met.*, 2022, **2022**, 1–11.

14 O. O. Salman, F. Brenne, T. Niendorf, J. Eckert, K. G. Prashanth, T. He and S. Scudino, *J. Manuf. Process.*, 2019, **45**, 255–261.
15 Y. Li, W. Li, F. S. L. Bobbert, K. Lietaert, J. H. Dong, M. A. Leeflang, J. Zhou and A. A. Zadpoor, *Acta Biomater.*, 2020, **106**, 439–449.
16 Q. Chen and G. A. Thouas, *Mater. Sci. Eng., R*, 2015, **87**, 1–57.
17 Y. F. Zheng, X. N. Gu and F. Witte, *Mater. Sci. Eng., R*, 2014, **77**, 1–34.
18 P. Wen, L. Jauer, M. Voshage, Y. Chen, R. Poprawe and J. H. Schleifenbaum, *J. Mater. Process. Technol.*, 2018, **258**, 128–137.
19 H. Pan, K. Pang, F. Cui, F. Ge, C. Man, X. Wang and Z. Cui, *Corros. Sci.*, 2019, **157**, 420–437.
20 F. Witte, *Acta Biomater.*, 2010, **6**, 1680–1692.
21 Z. Chun-Yan, Z. Rong-Chang, L. Cheng-Long and G. Jia-Cheng, *Surf. Coat. Technol.*, 2010, **204**, 3636–3640.
22 M. D. Pereda, C. Alonso, L. Burgos-Asperilla, J. A. Del Valle, O. A. Ruano, P. Perez and M. A. Fernández Lorenzo De Mele, *Acta Biomater.*, 2010, **6**, 1772–1782.
23 S. Hiromoto, T. Shishido, A. Yamamoto, N. Maruyama, H. Somekawa and T. Mukai, *Corros. Sci.*, 2008, **50**, 2906–2913.
24 J. E. Gray-Munro, C. Seguin and M. Strong, *J. Biomed. Mater. Res., Part A*, 2009, **91A**, 221–230.
25 E. Mostaed, M. Sikora-Jasinska, J. W. Drelich and M. Vedani, *Acta Biomater.*, 2018, **71**, 1–23.
26 Y. Su, I. Cockerill, Y. Wang, Y. X. Qin, L. Chang, Y. Zheng and D. Zhu, *Trends Biotechnol.*, 2019, **37**, 428–441.
27 J. Fu, Y. Su, Y. X. Qin, Y. Zheng, Y. Wang and D. Zhu, *Biomaterials*, 2020, **230**, 119641.
28 B. S. Moonga and D. W. Dempster, *J. Bone Miner. Res.*, 1995, **10**, 453–457.
29 H.-J. Seo, Y.-E. Cho, T. Kim, H.-I. Shin and I.-S. Kwun, *Nutr. Res. Pract.*, 2010, **4**, 356–361.
30 K. Praveenkumar, S. Swaroop and G. Manivasagam, *J. Mater. Eng. Perform.*, 2022, **31**, 6846–6857.
31 H. Yang, B. Jia, Z. Zhang, X. Qu, G. Li, W. Lin, D. Zhu, K. Dai and Y. Zheng, *Nat. Commun.*, 2020, **11**, 1–16.
32 P. K. Bowen, R. J. Guillory, E. R. Shearier, J. M. Seitz, J. Drelich, M. Bocks, F. Zhao and J. Goldman, *Mater. Sci. Eng., C*, 2015, **56**, 467–472.
33 C. K. Patrick Bowen, J. Drelich, J. Goldman, P. K. Bowen, J. Drelich and J. Goldman, *Adv. Mater.*, 2013, **25**, 2577–2582.
34 E. Jablonská, D. Vojtěch, M. Fousová, J. Kubásek, J. Lipov, J. Fojt and T. Ruml, *Mater. Sci. Eng., C*, 2016, **68**, 198–204.
35 T. Huang, Z. Liu, D. Wu and H. Yu, *J. Mater. Res. Technol.*, 2021, **15**, 226–240.
36 Y. Qin, P. Wen, D. Xia, H. Guo, M. Voshage, L. Jauer, Y. Zheng, J. H. Schleifenbaum and Y. Tian, *Addit. Manuf.*, 2020, **33**, 101134.
37 Z. Z. Shi, H. Y. Li, J. Y. Xu, X. X. Gao and X. F. Liu, *Materials Science and Engineering: A*, 2020, **771**, 138626.
38 Z. Z. Shi, J. Yu, X. F. Liu, H. J. Zhang, D. W. Zhang, Y. X. Yin and L. N. Wang, *Mater. Sci. Eng., C*, 2019, **99**, 969–978.
39 Z. Li, Z. Z. Shi, Y. Hao, H. F. Li, X. F. Liu, A. A. Volinsky, H. J. Zhang and L. N. Wang, *J. Mater. Sci. Technol.*, 2019, **35**, 2618–2624.
40 M. Salehi, S. Maleksaeedi, M. A. Bin Sapari, M. L. S. Nai, G. K. Meenashisundaram and M. Gupta, *Mater. Des.*, 2019, **169**, 107683.
41 G. Lu, Y. Dai, S. He, C. Chen, X. Liu, K. Tang, L. Guo, D. Zhang, J. Lin and C. Wen, *Corros. Sci.*, 2024, **239**, 112399.
42 W. Y. Li, Y. L. Dai, W. H. Cai, S. H. Lin, L. Guo, D. C. Zhang, Y. Li and C. Wen, *Rare Met.*, 2024, **43**, 5284–5304.
43 J. Lin, Y. Chen, Y. Dai, X. Zhang, D. Zhang, Y. Li and C. Wen, *Acta Biomater.*, 2025, **194**, 514–529.
44 M. Demirtas, G. Purcek, H. Yanar, Z. J. Zhang and Z. F. Zhang, *Mater. Sci. Eng., A*, 2015, **644**, 17–24.
45 Y. Zhu, J. Qin, J. Wang, P. Jin and P. Li, *Mater. Today Commun.*, 2023, **35**, 105670.
46 Q. Yang, D. L. Cheng, F. G. Zhang, Q. W. Shi, Z. Chen, M. L. Wang, S. Y. Zhong, Y. Wu and H. W. Wang, *Mater. Charact.*, 2021, **172**, 110825.
47 R. Rahmani, S. I. Lopes and K. G. Prashanth, *J. Funct. Biomater.*, 2023, **14**, 521.
48 R. Shukla, R. Sokkalingam and K. G. Prashanth, *J. Alloys Compd.*, 2023, 171079.
49 H. S. Maurya, J. Marczyk, K. Juhani, F. Sergejev, R. Kumar, A. Hussain, F. Akhtar, M. Hebda and K. G. Prashanth, *Mater. Today Adv.*, 2025, **25**, 100562.
50 L. Li, R. Li, T. Yuan, C. Chen, M. Wang, J. Yuan and Q. Weng, *J. Alloys Compd.*, 2020, **821**, 153520.
51 J. Čapek, E. Jablonská, J. Lipov, T. F. Kubatík and D. Vojtěch, *Mater. Chem. Phys.*, 2018, **203**, 249–258.
52 F. An, Z. Ma, K. Sun, L. Zhang, S. J. Na, J. Ning and H. Yu, *J. Mater. Res. Technol.*, 2023, **24**, 595–607.
53 J. Pinc, J. Čapek, J. Kubásek, F. Průša, V. Hybášek, P. Veřtát, I. Sedlářová and D. Vojtěch, *Metals*, 2020, **10**, 372.
54 Z. Zhang, Y. Yang, Y. Guo, Z. Xu, P. Sha, Z. Yu and L. Ren, *Surf. Coat. Technol.*, 2023, **466**, 129653.
55 M. K. Yadav, V. Pandey, K. Mohanta and V. K. Singh, *Ceram. Int.*, 2022, **48**(17), 25335–25345.
56 M. K. Yadav, V. Pandey, Jyoti, A. Kumar, K. Mohanta and V. K. Singh, *Ceram. Int.*, 2021, **47**(15), 22191–22200.
57 V. F. Dunskii, N. V. Nikitin and N. F. Tonkacheeva, *J. Eng. Phys.*, 1971, **20**, 558–560.
58 L. C. Zhang, W. Y. Xu, Z. Li, L. Zheng, Y. F. Liu and G. Q. Zhang, *Powder Technol.*, 2023, **418**, 118162.
59 M. Abedi, D. O. Moskovskikh, A. S. Rogachev and A. S. Mukasyan, *Metall. Mater. Trans. B*, 2016, **47**, 2725–2731.
60 D. Ovalı, M. Tarraste, M. Kaba, D. Ağaoğulları, L. Kollo, K. G. Prashanth and M. Lütfi Öveçoğlu, *Ceram. Int.*, 2021, **47**, 13827–13836.
61 N. Singh, R. Ummethala, P. S. P. S. Karamched, R. Sokkalingam, V. Gopal, G. Manivasagam and K. G. Prashanth, *J. Alloys Compd.*, 2021, **865**, 158875.
62 V. V. Patil, K. G. Prashanth and C. P. Mohanty, *J. Alloys Compd.*, 2023, **960**, 170734.

63 C. S. Bonifacio, J. F. Rufner, T. B. Holland and K. Van Benthem, *Appl. Phys. Lett.*, 2012, **101**, 093107.
64 M. Kermani, M. Razavi, M. R. Rahimipour and M. Zakeri, *J. Alloys Compd.*, 2014, **593**, 242–249.
65 D. Kumar, G. Shankar, K. G. Prashanth and S. Suwas, *Mater. Sci. Eng., A*, 2021, **820**, 141483.
66 D. Kumar, G. Shankar, K. G. Prashanth and S. Suwas, *J. Alloys Compd.*, 2023, 173040.
67 R. J. Vikram, L. Kollo, K. G. Prashanth and S. Suwas, *Metall. Mater. Trans. A*, 2021, **52**, 5329–5341.
68 K. G. Prashanth, S. Scudino, H. J. Klauss, K. B. Surreddi, L. Löber, Z. Wang, A. K. Chaubey, U. Kühn and J. Eckert, *Mater. Sci. Eng., A*, 2014, **590**, 153–160.
69 B. Hutchinson, J. Komenda, S. Kada, M. Barnett and A. Oskarsson, *Scr. Mater.*, 2019, **166**, 78–80.
70 D. H. StJohn, M. A. Easton, M. Qian, P. Cao and M. J. Birmingham, *Mater. Sci. Forum*, 2011, **690**, 206–209.
71 R. Chaim, *Mater. Sci. Eng., A*, 2007, **443**, 25–32.
72 Y. Cheng, Z. Cui, L. Cheng, D. Gong and W. Wang, *Adv. Powder Technol.*, 2017, **28**, 1129–1135.
73 G. Dirras, J. Gubicza, H. Couque, A. Ouarem and P. Jenei, *Mater. Sci. Eng., A*, 2013, **564**, 273–283.
74 M. Oghbaei and O. Mirzaee, *J. Alloys Compd.*, 2010, **494**, 175–189.
75 Z. A. Munir, U. Anselmi-Tamburini and M. Ohyanagi, *J. Mater. Sci.*, 2006, **41**, 763–777.
76 Z. Wang, K. G. Prashanth, K. B. Surreddi, C. Suryanarayana, J. Eckert and S. Scudino, *Materialia*, 2018, **2**, 157–166.
77 K. B. Surreddi, S. Scudino, M. Sakaliyska, K. G. Prashanth, D. J. Sordelet and J. Eckert, *J. Alloys Compd.*, 2010, **491**, 137–142.
78 G. Liu, R. Li, T. Yuan, M. Zhang and F. Zeng, *Int. J. Refract. Met. Hard Mater.*, 2017, **66**, 68–75.
79 A. Flaureau, A. Weibel, G. Chevallier and C. Estournès, *J. Eur. Ceram. Soc.*, 2021, **41**, 3581–3594.
80 H. Li, Q. Q. Duan, X. W. Li and Z. F. Zhang, *Mater. Sci. Eng., A*, 2007, **466**, 38–46.
81 Y. Xin, X. Zhou, L. Lv and Q. Liu, *Mater. Sci. Eng., A*, 2014, **606**, 81–91.
82 S. Yu, H. Chi, P. Li, B. Guo, Z. Yu, Z. Xu, P. Liang, Z. Zhang, Y. Guo and L. Ren, *Addit. Manuf.*, 2024, **93**, 104411.
83 P. K. Bowen, E. R. Shearier, S. Zhao, R. J. Guillory, F. Zhao, J. Goldman and J. W. Drelich, *Adv. Healthcare Mater.*, 2016, **5**, 1121–1140.
84 L. Liu, Y. Meng, C. Dong, Y. Yan, A. A. Volinsky and L. N. Wang, *J. Mater. Sci. Technol.*, 2018, **34**, 2271–2282.
85 X. Liu, Y. Cheng, Z. Guan and Y. Zheng, *Corros. Sci.*, 2020, **170**, 108661.
86 Q. Cui, D. Yi, H. Wang, J. Zhang, J. Xu and B. Wang, *J. Rare Earths*, 2019, **37**, 1341–1350.
87 P. Wang, L. Ma, X. Cheng, X. Li, L. Wang, C. Dong, C. Man, Y. Hu, Q. Yu, J. Ma, F. Feng, B. Yu, H. Chen, B. Yu, H. Yan, Q. Wu, Z. Hu, F. Chen, Y. Wei, Y. Fu, Z. Pan, Y. Ma, H. Cheng, Q. Zhao, H. Luo, Z. Wang, Z. Zheng, L. Zhao, Y. Lei and K. Yang, *Int. J. Miner., Metall. Mater.*, 2021, **28**, 1112–1126.
88 M. Amirnejad, M. Rajabi and R. Jamaati, *Corros. Sci.*, 2021, **179**, 109100.
89 R. Soni, S. Jhavar, S. Tyeb, S. K. Gupta, S. Suwas and K. Chatterjee, *J. Funct. Biomater.*, 2022, **13**, 212.
90 M. H. Qi, J. L. Xu, T. Lai, J. Huang, Y. C. Ma, J. M. Luo and Y. F. Zheng, *J. Alloys Compd.*, 2023, **931**, 167555.
91 H. Yang, X. Qu, W. Lin, C. Wang, D. Zhu, K. Dai and Y. Zheng, *Acta Biomater.*, 2018, **71**, 200–214.
92 X. Tong, D. Zhang, X. Zhang, Y. Su, Z. Shi, K. Wang, J. Lin, Y. Li, J. Lin and C. Wen, *Acta Biomater.*, 2018, **82**, 197–204.
93 S. C. P. Cachinho and R. N. Correia, *J. Mater. Sci.: Mater. Med.*, 2008, **19**, 451–457.
94 M. A. Amin, K. F. Khaled and S. A. Fadl-Allah, *Corros. Sci.*, 2010, **52**, 140–151.
95 Z. Shi, M. Liu and A. Atrens, *Corros. Sci.*, 2010, **52**, 579–588.
96 E. Poorqasemi, O. Abootalebi, M. Peikari and F. Haqdar, *Corros. Sci.*, 2009, **51**, 1043–1054.
97 P. F. Ji, B. Li, B. H. Chen, F. Wang, W. Ma, X. Y. Zhang, M. Z. Ma and R. P. Liu, *Corros. Sci.*, 2020, **170**, 108696.
98 R. Soni, S. Jhavar, S. Tyeb, S. K. Gupta, S. Suwas and K. Chatterjee, *J. Funct. Biomater.*, 2022, **13**(4), 212.
99 D. Vojtěch, J. Kubásek, J. Šerák and P. Novák, *Acta Biomater.*, 2011, **7**, 3515–3522.
100 E. Koç, M. B. Kannan, M. Ünal and E. Candan, *J. Alloys Compd.*, 2015, **648**, 291–296.
101 M. H. Qi, J. L. Xu, T. Lai, J. Huang, Y. C. Ma, J. M. Luo and Y. F. Zheng, *J. Alloys Compd.*, 2023, **931**, 167555.
102 J. Čapek, E. Jablonská, J. Lipov, T. F. Kubatík and D. Vojtěch, *Mater. Chem. Phys.*, 2018, **203**, 249–258.
103 J. Pinc, J. Čapek, J. Kubásek, F. Průša, V. Hybášek, P. Veřtát, I. Sedlářová and D. Vojtěch, *Metals*, 2020, **10**(3), 372.
104 H. Yang, X. Qu, W. Lin, C. Wang, D. Zhu, K. Dai and Y. Zheng, *Acta Biomater.*, 2018, **71**, 200–214.
105 S. Huang, L. Chen, B. Jiang, L. Qiao and Y. Yan, *J. Electroanal. Chem.*, 2021, **886**, 115145.
106 L. Upadhayay, S. Nilawar, C. Kumar, K. Chatterjee and P. Kumar, *J. Mater. Sci.*, 2024, **59**, 5872–5890.